

Induced Scattering of Fast Radio Bursts in Magnetar Magnetospheres

Rei Nishiura^{DOI*}

Department of Physics, Kyoto University, Kyoto 606-8502, Japan

Shoma F. Kamijima^{DOI†} and Kunihito Ioka^{DOI‡}

Center for Gravitational Physics and Quantum Information,
Yukawa Institute for Theoretical Physics, Kyoto University, Kyoto 606-8502, Japan

(Dated: January 28, 2026)

We investigate induced Compton/Brillouin scattering of electromagnetic waves in magnetized electron and positron pair plasma by verifying kinetic theory with Particle-in-Cell simulations. Applying this to fast radio bursts (FRBs) in magnetar magnetospheres, we find that the scattering—although suppressed by the magnetic field—inevitably enters the linear growth stage. The subsequent evolution bifurcates: full scattering occurs when the density exceeds a critical value, whereas below it the scattering saturates and the FRB can escape. This eases the tension with observations of compact emission regions and may explain the observed diversity, including the presence or absence of FRBs associated with X-ray bursts.

Introduction Fast radio bursts (FRBs) are the brightest radio transients, first discovered in 2007 [1]. Most FRBs are extragalactic, and their progenitors and radiation mechanisms remain unresolved. The simultaneous detection in 2020 of FRB 20200428 with X-ray bursts from a Galactic magnetar established magnetars as at least one class of FRB sources [2–4].

Nonlinear interactions between large-amplitude electromagnetic (EM) waves and plasma are central in both astrophysical and laboratory environments, such as the Sun [5–16], FRBs [17–19], pulsars [20–25], laser–plasma interactions [26–30] and free electron lasers [31, 32]. Parametric instability redistributes the incident wave energy into scattered waves and plasma through the beat of these waves, as illustrated in Fig. 1. Among such processes, we collectively refer to induced Compton scattering (ICS), stimulated Brillouin scattering (SBS), and stimulated Raman scattering (SRS) as *induced scattering*. ICS denotes coupling between the beat and particle thermal motion via Landau resonance, whereas SBS and SRS are three-wave resonances, in which the beat couples to an acoustic wave and a Langmuir wave, respectively.

A key theoretical concern for magnetar FRBs is that induced scattering may attenuate emission within the magnetosphere so strongly that the radiation cannot escape [19, 33–42]. On the other hand, several observations imply that the source size of FRBs is comparable to the magnetosphere [43–45], leaving tension between theoretical expectations and observation.

Despite this importance, induced scattering in strongly magnetized plasma is not fully understood [19, 46–53]. Nishiura *et al.* [42, 54] first developed a kinetic framework of induced scattering in strongly magnetized e^\pm plasma and identified three density fluctuation modes, *the ordinary, neutral, and charged modes*. They also showed that ICS, SBS, and SRS can compete with one another.

In the follow-up work, Kamijima *et al.* [55] used a one-dimensional Particle-in-Cell (PIC) simulation of a circu-

larly polarized Alfvén wave. This simulation clarified two key points. First, it confirmed the linear growth rates of neutral ICS and charged ICS predicted by [42, 54] and verified that the dominant channel switches as the plasma parameters are varied. Second, it followed the nonlinear evolution beyond the linear growth stage and showed that, in some cases, the instability saturates while the incident wave energy is hardly damped.

In this work, we first use the same PIC simulation scheme as [55] to clarify the overall picture of induced scattering. In particular, we reproduce the ICS–SBS transition of the neutral mode predicted by [54] and discover a nonlinear evolution leading to full scattering of the incident wave without saturation, unlike in [55]. Furthermore, by combining the linear and nonlinear results, we show that FRBs can be either strongly attenuated or escape freely from the magnetosphere, potentially explaining their observed diversity.

Summary of the kinetic theory of induced scattering
In this section, we summarize the kinetic theory of induced scattering for an incident EM wave whose electric field \mathbf{E}_{w0} is perpendicular to the strong background magnetic field \mathbf{B}_0 in the high density regime $\omega_0 \sim \omega_1 \ll \omega_p \ll \omega_c$, that is appropriate for magnetar magnetospheres [42, 54]. Here ω_0 and ω_1 are the frequencies of the incident and scattered waves, $\omega_c \equiv eB_0/(m_e c)$ is the cyclotron frequency, and $\omega_p \equiv \sqrt{8\pi e^2 n_{e0}/m_e}$ is the plasma frequency. The polarization $\mathbf{E}_{w0} \perp \mathbf{B}_0$ corresponds to a fast magnetosonic wave that propagates in an arbitrary direction or to an Alfvén wave with wave vector $\mathbf{k}_0 \parallel \mathbf{B}_0$. In contrast, an EM pulse with $\mathbf{E}_{w0} \parallel \mathbf{B}_0$ does not propagate because of the cutoff [42, 54]. We assume that the motion of the charged particles in the plasma is nonrelativistic and can be characterized by

$$\eta_{\text{inci}} \equiv \frac{B_{\text{inci}}}{B_0} = a_e \frac{\omega_0}{\omega_c} \left(1 + \frac{\omega_p^2}{\omega_c^2} \right)^{\frac{1}{2}} \ll 1, \quad (1)$$

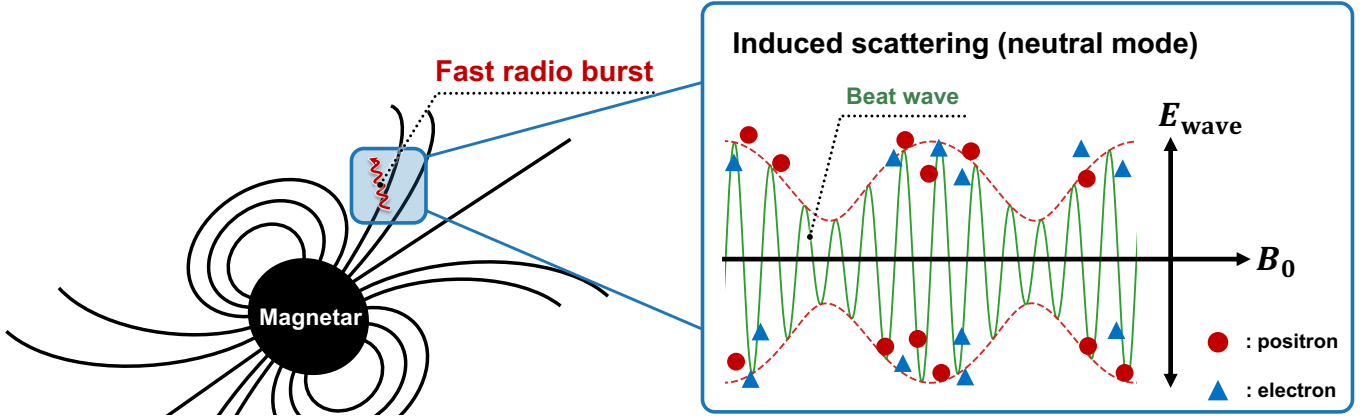


FIG. 1: Schematic illustration of neutral-mode induced scattering of an FRB in a magnetar magnetosphere.

where $|\mathbf{B}_{w0}| \equiv B_{\text{inci}}$ is the incident magnetic amplitude and $a_e \equiv eE_{\text{inci}}/(m_e c \omega_0)$ is the strength parameter.

We refer to [54] for details of the kinetic framework and summarize here only the key elements. The framework is based on the Vlasov equation for distribution functions $f_{\pm}(\mathbf{r}, \mathbf{v}, t) = f_0(\mathbf{v}) + \delta f_{\pm}(\mathbf{r}, \mathbf{v}, t)$ including the ponderomotive potential generated by the beat wave,

$$\frac{\partial f_{\pm}}{\partial t} + \mathbf{v} \cdot \nabla f_{\pm} + \left[-\nabla \phi_{\text{p}}^{\pm} \pm e \left(\mathbf{E} + \frac{\mathbf{v} \times \mathbf{B}_0}{c} \right) \right] \cdot \frac{\partial f_{\pm}}{\partial \mathbf{p}} = 0, \quad (2)$$

and is solved together with the Maxwell equations $\nabla \cdot \mathbf{E} = \sum_{q=\pm e} 4\pi q n_{e0} \int \delta f_{\pm} d^3 \mathbf{v}$. Here $+$ ($-$) denotes a positron (electron), and the equilibrium distribution $f_0(\mathbf{v})$ is assumed to be Maxwellian. The ponderomotive potential is expressed as [56–61]

$$\phi_{\text{p}}^{\pm} = \frac{e^2}{2m_e} \left\langle -\frac{|\mathbf{E}_{w\perp}|^2}{\omega_c^2 - \omega_0^2} \pm i \frac{\omega_c \hat{\mathbf{B}}_0 \cdot (\mathbf{E}_{w\perp}^* \times \mathbf{E}_{w\perp})}{\omega_0(\omega_0^2 - \omega_c^2)} \right\rangle, \quad (3)$$

where $\omega_1 \sim \omega_0 \gg |\omega|$, the time average is taken over a timescale longer than ω_0^{-1} and shorter than $|\omega|^{-1}$, and $\omega \equiv \omega_1 - \omega_0$ is the density fluctuation frequency. The first term in Eq. (3) drives the neutral mode and the second term drives the charged mode. As illustrated in Fig. 1, the neutral mode excites a density fluctuation independent of the charge sign, similar to the unmagnetized case, whereas the charged mode excites a density fluctuation accompanied by charge separation, which is distinct from the unmagnetized case.

Linearizing Eq. (2) yields the dispersion relation and the linear growth rate of the scattered wave and the density fluctuation, which we define as $t^{-1} \equiv 2 \text{Im } \omega_1 = 2 \text{Im } \omega$. The neutral mode exhibits a continuous transition from ICS to SBS as the incident amplitude $a_e \omega_0 / \omega_c$ increases. $(t_{\text{neutral}}^{\text{coh}})^{-1} \propto a_e^2$ in the ICS regime and $(t_{\text{neutral}}^{\text{coh}})^{-1} \propto a_e^{\frac{2}{3}}$ in the SBS regime. The precise expression for the maximum linear growth rate, together with the transition amplitude $(a_e \omega_0 / \omega_c)^{\text{coh}}_{\text{trans}}$, is summarized in Eqs. (A.7) and (A.8). The maximum growth

occurs when an EM wave incident along \mathbf{B}_0 that undergoes 180° backward scattering [42, 54]. Compared with the unmagnetized case, the growth rate is suppressed by a factor of $(\omega_0 / \omega_c)^4$ for ICS and by $(\omega_0 / \omega_c)^{\frac{4}{3}}$ for SBS, which can be interpreted as a gyroradius effect [42, 54].

PIC simulation setup We verify the linear growth rate of ICS driven by a circularly polarized Alfvén incident wave in magnetized e^{\pm} plasma using the same PIC simulation scheme as in the companion paper Kamiyama *et al.* [55]. We adopt plasma parameters that differ from those in [55] so that the dominant induced scattering process changes. The magnetization of the e^{\pm} plasma is set to $\sigma_B \equiv B_0^2 / (8\pi n_{e0} m_e c^2) = \omega_c^2 / \omega_p^2 = 2$, the normalized incident frequency is $\omega_0 / \omega_p = 7.1 \times 10^{-2}$, and the thermal velocity of electrons and positrons is $\sqrt{k_B T_e / (m_e c^2)} = 0.04$. The spatial resolution of the incident wavelength is $\lambda_0 / \Delta x = 1200$, and the simulation box size is $2\Delta x \times 32\lambda_0$ in the $(x \times y)$ directions, so that $L_y \gg L_x$ and the system effectively follows one-dimensional propagation along \mathbf{B}_0 (see Fig. 2 in [55]). This box size comfortably satisfies the resolution requirement for the scattered wavenumber, $L_y / \lambda_0 \gtrsim 13$. The background magnetic field is set to $\mathbf{B}_0 \parallel \hat{\mathbf{y}}$, and the incident field is a right-handed (electron-like) circularly polarized Alfvén wave with $\mathbf{k}_0 \parallel \mathbf{B}_0$.

PIC simulation results Fig. 2 shows that the maximum linear growth rate of the neutral mode agrees with the analytic expressions in Eq. (A.7), with the solution of the dispersion relation (Eq. (21) of [54]), and with the PIC measurements, and that it increases smoothly from ICS to SBS as $\eta_{\text{inci}}^{\text{circ}}$ grows. Although the SBS growth rate is larger than that of ICS on the small $\eta_{\text{inci}}^{\text{circ}}$ side, SBS is not realized because the acoustic wave in e^{\pm} plasma is a heavily Landau-damped quasi-mode [54]. The deviations from the dispersion relation solution are only 16–28% across all points.

The PIC simulation reveals the nonlinear evolution beyond the linear growth stage. For the small values of $\eta_{\text{inci}}^{\text{circ}}$ in Fig. 2, corresponding to the leftmost five points, the

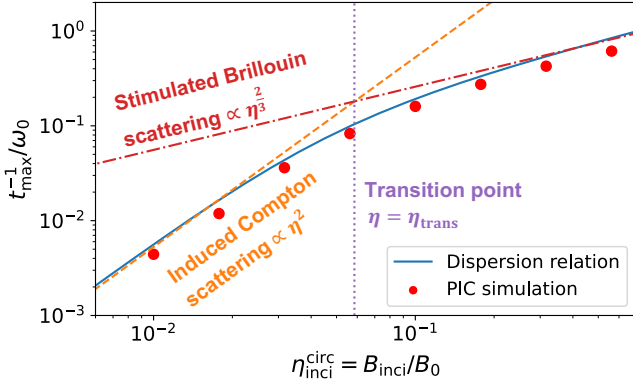


FIG. 2: Maximum linear growth rate of induced scattering driven by the neutral mode for a monochromatic incident wave as a function of the incident wave amplitude $\eta_{\text{inci}}^{\text{circ}}$. Red dots denote the PIC results. The blue solid curve is the numerical solution of the dispersion relation of the neutral mode (see Eq. (21) of [54]). The orange dashed and red dash-dotted curves are the analytic ICS and SBS in Eq. (A.7), respectively. The purple dotted curve shows the ICS–SBS transition amplitude obtained from Eq. (A.8) rewritten using Eq. (1).

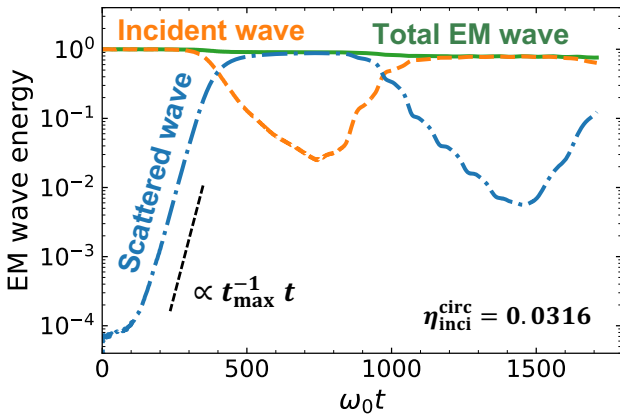


FIG. 3: Time evolution of the forward and backward components of the EM wave energy, normalized by the initial incident wave energy. The horizontal axis is time normalized by ω_0 , and the vertical axis is the EM wave energy Fourier-transformed along \mathbf{B}_0 (see [55] for the detailed treatment of the Fourier transformation). The forward right-handed circularly polarized Alfvén waves (orange dashed) are initially injected, and the scattered components (blue dot-dashed) are the backward right-handed circularly polarized Alfvén waves generated by induced scattering. The green solid curve shows the total EM wave energy, and the black dashed line indicates the slope corresponding to the maximum linear ICS growth rate of the neutral mode in Eq. (A.7).

forward and backward components undergo oscillatory energy exchange, as shown in Fig. 3. At early times, the backward waves grow in accordance with the linear growth rate in Eq. (A.7). The total EM wave energy decreases because it is transferred to the internal energy of the plasma, but the decrease is small. The backward waves then grow until they reach an energy comparable to that of the forward wave, while the forward wave is strongly attenuated. Subsequently, the roles of the two components are exchanged. The forward waves (granddaughter waves) increase again, whereas the backward waves decrease. Note that the frequency and wavenumber of the granddaughter waves differ from those of the incident wave. Although the total EM wave energy appears to be nearly conserved within a local simulation box, an FRB propagates through fresh scattering regions, so the local energy exchange cannot complete an oscillation cycle in each region. On average, the FRB is strongly damped, and we refer to this case as *full scattering*.

In contrast, the three largest values of $\eta_{\text{inci}}^{\text{circ}}$ in Fig. 2 show a qualitatively different evolution. The scattered wave initially grows linearly, but then saturates, and no oscillatory energy exchange is observed. We refer to this behavior as *partial scattering*. A similar low-level saturation is seen in Fig. 5 of [55] for different parameters.

Induced scattering saturates when a plateau forms in the plasma distribution function around the phase velocity of the beat wave [55]. The distribution function evolves according to the Vlasov equation (2), in which the ponderomotive force enters as $-(1/m_e) \nabla \phi_p^\pm \cdot (\partial \mathbf{f}_\pm / \partial \mathbf{v})$. As the instability grows, it flattens the slope of the distribution function near the phase velocity of the beat wave. As the slope becomes shallower and eventually approaches a plateau, the ponderomotive force can no longer sustain the instability, and the system saturates. This is essentially for the same reason that Landau damping saturates once the distribution function flattens into a plateau [62, 63].

A plateau is expected to form once the EM wave deposits an energy density comparable to the internal energy density of the plasma. The internal energy density is estimated as $\varepsilon_{\text{th}} = 2n_e \cdot \frac{1}{2} k_B T_e$ since only the velocity along \mathbf{B}_0 enters the resonance and the effective degree of freedom is 1. In a single scattering event, energy conservation implies that an incident wave with energy ω_0 transfers an energy fraction ω_1 to the scattered wave and a fraction $|\omega_1 - \omega_0|$ to the plasma. Then the energy density of the scattered wave at saturation is estimated as

$$\varepsilon_{\text{scat}}^{\text{max}} \sim \frac{\omega_1}{|\omega_1 - \omega_0|} \varepsilon_{\text{th}}. \quad (4)$$

For ICS, Eq. (30) of [55] yields $\varepsilon_{\text{scat}}^{\text{max}} \sim \frac{1}{2} \frac{v_A}{c} \left(\frac{m_e c^2}{k_B T_e} \right)^{\frac{1}{2}} \varepsilon_{\text{th}}$, where $v_A \equiv c(1 + \omega_p^2/\omega_c^2)^{-\frac{1}{2}}$ is the Alfvén speed. For SBS, the angular frequency of the density fluctuation $\omega_1 - \omega_0$ is derived in Eq. (C6) of [54]. Taking its real part and

using $\omega_1 \sim \omega_0$, one obtains $\varepsilon_{\text{scat}}^{\max} \sim 2\sigma_B^{\frac{1}{3}}\eta_{\text{inc}}^{-\frac{2}{3}}\varepsilon_{\text{th}}$. PIC simulations confirm that Eq. (4) is consistent with the saturation condition to within a factor of a few, and a detailed paper is in preparation.

Linear growth rates for a broadband incident wave In the PIC simulations, we adopted a monochromatic incident wave. When applying our results to FRBs, however, it is necessary to account for the finite bandwidth $\Delta\omega$ of the incident wave. Some FRBs exhibit broadband emission with $\Delta\omega \sim \omega_0$ [64], and we therefore consider broadband incident waves. Finite bandwidth reduces phase coherence between the incident and scattered waves and weakens the effective three wave resonance. This reduction lowers the maximum linear growth rate relative to the monochromatic limit [65–69]. For the neutral mode, the growth rate scales as $(t_{\text{neutral}}^{\text{broad}})^{-1} \propto a_e^2 \Delta\omega^{-2}$ in the ICS regime and as $(t_{\text{neutral}}^{\text{broad}})^{-1} \propto a_e^{\frac{4}{3}} \Delta\omega^{-1}$ in the SBS regime. The explicit growth rate formulae and the ICS–SBS transition amplitude are summarized in Eqs. (A.9) and (A.10).

For the charged mode, the behavior of induced scattering depends strongly on the plasma density [54]. In the regime $\omega_0 \ll \omega_p \ll \omega_c$, ICS with Debye screening is the dominant process. The corresponding maximum linear growth rate for a broadband incident wave is listed in Eq. (A.11), and scales as $(t_{\text{charged}}^{\text{broad}})^{-1} \propto a_e^2 \Delta\omega^{-2}$. Compared with the unmagnetized case, the linear growth rate is suppressed not only by the gyro-radius effect $(\omega_0/\omega_c)^2$ but also by the Debye screening effect $(\omega_0/\omega_p)^4 (8k_B T_e / (m_e c^2))^2 (1 + \omega_p^2/\omega_c^2)^2$ [42].

Application to extragalactic FRBs We now apply the above framework to GHz FRBs propagating as fast magnetosonic waves in a dipolar magnetar magnetosphere and summarize the main result in Fig. 4. For a dipole field, the magnetic field strength at radius r can be expressed in terms of the polar surface field B_p as $B(r) \sim B_p R^3/r^3 \sim 10^8 \text{ G } r_8^{-3} R_6^3 B_{p,14}$, and the plasma density is given by the Goldreich–Julian density [70] multiplied by the pair multiplicity \mathcal{M} , $n(r) \equiv \mathcal{M} n_{\text{GJ}}(r) \sim \mathcal{M} B(r)/(ceP) \sim 6.9 \times 10^{14} \text{ cm}^{-3} P^{-1} r_8^{-3} R_6^3 B_{p,14} \mathcal{M}_8$. Here R and P are the magnetar radius and rotation period, and we use the notation $A \equiv 10^n A_n$ in CGS units and $T_{80\text{keV}} \equiv T/80\text{keV}$ for temperatures. Once $B(r)$ and $n(r)$ are specified, the cyclotron and plasma frequencies are determined. We consider an FRB with central frequency $\nu_0 = \omega_0/(2\pi)$, bandwidth $\Delta\nu$, duration Δt , and Poynting luminosity $L \equiv 4\pi r^2 v_A (|\mathbf{E}_w|^2 + |\mathbf{B}_w|^2)/(8\pi)$. The strength parameter is then given by $a_e = 2eL^{\frac{1}{2}}(1 + c^2/v_A^2)^{-\frac{1}{2}}/(m_e c v_A^{\frac{1}{2}} \omega_0 r) \simeq 2.3 \times 10^4 r_8^{-1} L_{40}^{\frac{1}{2}} \nu_9^{-1}$. Since $\omega_p/\omega_c = 1/\sqrt{\sigma_B} \sim 1.2 \times 10^{-3} \mathcal{M}_8^{\frac{1}{2}} r_8^{\frac{3}{2}} P^{-\frac{1}{2}} R_6^{-\frac{3}{2}} B_{p,14}^{-\frac{1}{2}}$, the subluminal effect $(1 + \omega_p^2/\omega_c^2) = (c/v_A)^2 \sim 1$ can be neglected. Once a_e is specified, the dimensionless amplitude of the FRB is obtained as $\eta \simeq a_e \omega_0 / \omega_c \simeq 8.2 \times 10^{-2} r_8^2 L_{40}^{\frac{1}{2}} B_{p,14}^{-1} R_6^{-3}$. Since $\eta \propto r^2$, η becomes larger

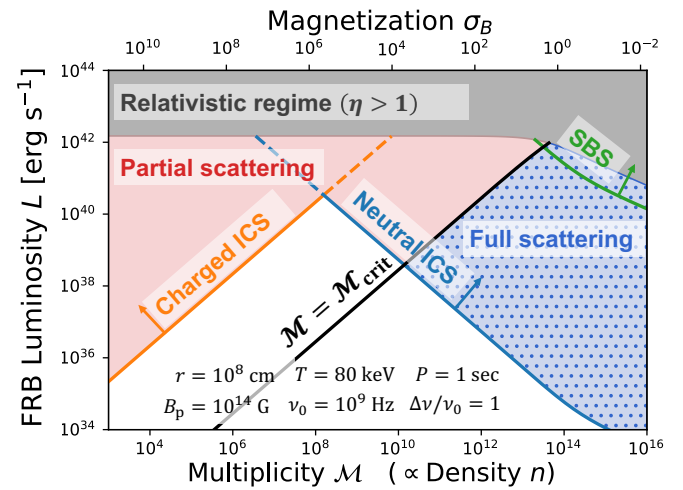


FIG. 4: Regime map of induced scattering for GHz FRB pulses propagating through a dipolar magnetar magnetosphere. The horizontal axis shows the multiplicity \mathcal{M} , and the top axis shows the corresponding magnetization parameter σ_B . The vertical axis shows the FRB Poynting luminosity L . Colored/shaded regions indicate partial scattering (red), full scattering (blue hatched), and the relativistic regime $\eta > 1$ (gray). The dominant process in each region is labeled as “Neutral ICS,” “Charged ICS,” or “(Neutral) SBS”.^a The black curve marks the boundary between partial and full scattering. The parameters used in this figure are listed in the panel.

^a At high \mathcal{M} ($\sigma_B \lesssim 1$), the curves bend because the subluminal correction $(1 + \omega_p^2/\omega_c^2) = (c/v_A)^2$ becomes non-negligible.

at larger radii, and our analysis remains applicable as long as $\eta < 1$ is satisfied.

Note that the region below the green SBS curve in Fig. 4 can be treated only with the kinetic treatment developed in this work rather than fluid treatment. The condition for the dominant induced scattering in the neutral mode to be ICS rather than fluid-type SBS is from Eq. (A.10), $\mathcal{M} < 2.3 \times 10^{15} P R_6^9 B_{p,14}^3 r_8^{-7} L_{40}^{-1} (\Delta\nu/\nu_0)^3$. As shown in Fig. 2, extrapolating the SBS growth rate into this ICS-dominated region would overestimate the growth rate by several orders of magnitude.

The maximum linear growth rates of the charged and neutral modes for a broadband FRB (Eqs. (A.11) and the ICS regime of (A.9)) are estimated as

$$(t_{\text{charged}}^{\text{broad}})^{-1} \approx 4.6 \times 10^2 \text{ s}^{-1} \frac{P r_8^7 L_{40} T_{80\text{keV}}^2 \nu_9^3}{\mathcal{M}_8 R_6^9 B_{p,14}^3} \left(\frac{\Delta\nu}{\nu_0} \right)^{-2},$$

$$(t_{\text{neutral}}^{\text{broad}})^{-1} \approx 1.9 \times 10^2 \text{ s}^{-1} \frac{\mathcal{M}_8 r_8^7 L_{40} \nu_9}{P R_6^9 B_{p,14}^3} \left(\frac{\Delta\nu}{\nu_0} \right)^{-2}, \quad (5)$$

and we compare these with a typical FRB inverse duration $\Delta t^{-1} \sim 10^3 \text{ s}^{-1}$. In Fig. 4, the red and blue hatched regions at $r = 10^8 \text{ cm}$ show where $(t^{\text{broad}})^{-1} > \Delta t^{-1}$,

i.e., FRBs enter the linear growth stage of induced scattering in at least one mode. The linear growth region expands at larger r , and we can show that typical FRBs with $L \sim 10^{38-42}$ erg s $^{-1}$ always enter the linear growth stage before $\eta = 1$, irrespective of \mathcal{M} .

At first glance, most FRBs would appear to be strongly scattered. However, our results indicate a wide parameter region where induced scattering saturates, so that FRBs undergo only partial scattering. This occurs when the total FRB energy exceeds the saturation energy of the scattered wave in Eq. (4). The total energy of an FRB is written as $\mathcal{E}_{\text{FRB}} = L\Delta t \sim 10^{37}$ erg $L_{40}\Delta t_{-3}$. The saturation energy of the scattered wave at radius r is obtained from Eq. (4) and is estimated as $\mathcal{E}_{\text{scat}}^{\text{max}} \sim 4\pi r^2 \Delta r \varepsilon_{\text{scat}}^{\text{max}} \sim 4\pi r^3 \varepsilon_{\text{scat}}^{\text{max}}$. Therefore, the condition $\mathcal{E}_{\text{FRB}} > \mathcal{E}_{\text{scat}}^{\text{max}}$ implies partial scattering, while $\mathcal{E}_{\text{FRB}} \leq \mathcal{E}_{\text{scat}}^{\text{max}}$ implies full scattering. At the boundary $\mathcal{E}_{\text{FRB}} = \mathcal{E}_{\text{scat}}^{\text{max}}$, this criterion can be written, for ICS, as a critical luminosity, $L_{\text{crit}} \sim \frac{2\pi r^3 n(r) m_e c^2}{\Delta t} \sqrt{\frac{k_B T_e}{m_e c^2}}$, so that solving for $n(r)$ yields the critical multiplicity shown by the black solid curve in Fig. 4, and it is calculated as

$$\mathcal{M}_{\text{crit}} \equiv \frac{1}{6} \frac{L\Delta t}{\frac{4\pi r^3}{3} \frac{B(r)^2}{8\pi}} \frac{\omega_c(r)}{\Omega} \sqrt{\frac{m_e c^2}{k_B T_e}} \sim 7.1 \times 10^{11} \frac{L_{40} P \Delta t_{-3}}{R_6^3 B_{p,14} T_{80\text{keV}}}.$$
(6)

The large $\mathcal{M}_{\text{crit}}$ arises because the ratio $\omega_c(r)/\Omega$ is large, where $\Omega \equiv 2\pi/P$ is the angular velocity of the magnetar. Although this density is naively Thomson thick, Thomson scattering for GHz EM waves with $\mathbf{E}_{w0} \perp \mathbf{B}_0$ is suppressed by $(\omega_0/\omega_c)^2$ [40].

Discussions Our results have important observational implications. Whether FRBs can escape magnetar magnetospheres depends on the plasma density. For typical FRB luminosities $L \sim 10^{38-42}$ erg/s, the waves generally enter the linear growth stage of ICS irrespective of density, but if the plasma density is not extremely dense, $\mathcal{M} < \mathcal{M}_{\text{crit}} = 7.1 \times 10^{11} L_{40} P \Delta t_{-3} R_6^{-3} B_{p,14}^{-1} T_{80\text{keV}}^{-1}$, induced scattering can saturate and the FRB can escape with little attenuation. This is consistent with observational indications that some extragalactic FRBs have compact source sizes comparable to magnetar magnetospheres [43–45]. In contrast, for magnetar giant flares, observations suggest that a large amount of matter is ejected [71–73], implying a high-density region $\sigma_B \sim 1$ where full scattering is consistent with the non-detection of associated FRBs. A similar argument applies when a fireball forms during magnetar bursts [74–76]. The plasma density can become high, $\mathcal{M} > \mathcal{M}_{\text{crit}}$, so the system enters the full scattering regime and the FRB is strongly damped. This may explain why most X-ray bursts lack accompanying FRBs [77, 78].

Future work should address competition with other parametric instabilities, including interactions between

Alfvén and fast magnetosonic waves [79–82]. The relativistic regime $\eta > 1$ is also beyond the scope of this work and requires future theoretical studies. Applying the present framework to the propagation of pulsar radio emission [21, 23, 24] and to precursor emission from neutron star mergers [83–86] is another important direction.

We gratefully acknowledge insightful discussions with Masanori Iwamoto, Jonathan Granot, Wataru Ishizaki, Takashi Hosokawa. RN is supported by JST SPRING, Grant No. JPMJSP2110, and JSPS KAKENHI, Grant No. 25KJ1562. KI is supported by MEXT/JSPS KAKENHI Grant No.23H01172, 23H05430, 23H04900, 22H00130. SK is supported by MEXT/JSPS KAKENHI Grant No.22H00130 and 23K20038. Numerical computations were carried out on Cray XC50 and XD2000 at Center for Computational Astrophysics, National Astronomical Observatory of Japan, Yukawa-21 at YITP in Kyoto University, and Flow in Nagoya University through the HPCI System Research Project (Project ID: hp240147, hp250036) The authors thank the Yukawa Institute for Theoretical Physics at Kyoto University, where this work was further developed during the YITP-W-25-08 on "Exploring Extreme Transients: Frontiers in the Early Universe and Time-Domain Astronomy".

* nishiura@tap.scphys.kyoto-u.ac.jp

† shoma.kamijima@yukawa.kyoto-u.ac.jp

‡ kunihito.ioka@yukawa.kyoto-u.ac.jp

- [1] D. R. Lorimer, M. Bailes, M. A. McLaughlin, D. J. Narkevic, and F. Crawford, *Science* **318**, 777 (2007), arXiv:0709.4301 [astro-ph].
- [2] CHIME/FRB Collaboration, B. C. Andersen, K. M. Bandura, M. Bhardwaj, A. Bij, M. M. Boyce, P. J. Boyle, C. Brar, T. Cassanelli, P. Chawla, T. Chen, J. F. Cliche, A. Cook, D. Cubranic, A. P. Curtin, N. T. Denman, M. Dobbs, F. Q. Dong, M. Fandino, E. Fonseca, B. M. Gaensler, U. Giri, D. C. Good, M. Halpern, A. S. Hill, G. F. Hinshaw, C. Höfer, A. Josephy, J. W. Kania, V. M. Kaspi, T. L. Landecker, C. Leung, D. Z. Li, H. H. Lin, K. W. Masui, R. McKinven, J. Mena-Parra, M. Merryfield, B. W. Meyers, D. Michilli, N. Milutinovic, A. Mirhosseini, M. Müncmeyer, A. Naidu, L. B. Newburgh, C. Ng, C. Patel, U. L. Pen, T. Pinsonneault-Marotte, Z. Pleunis, B. M. Quine, M. Rafiei-Ravandi, M. Rahman, S. M. Ransom, A. Renard, P. Sanghavi, P. Scholz, J. R. Shaw, K. Shin, S. R. Siegel, S. Singh, R. J. Smegal, K. M. Smith, I. H. Stairs, C. M. Tan, S. P. Tendulkar, I. Tretyakov, K. Vanderlinde, H. Wang, D. Wulf, and A. V. Zwaniga, *Nature* **587**, 54 (2020), arXiv:2005.10324 [astro-ph.HE].
- [3] C. D. Bochenek, V. Ravi, K. V. Belov, G. Hallinan, J. Kocz, S. R. Kulkarni, and D. L. McKenna, *Nature* **587**, 59 (2020), arXiv:2005.10828 [astro-ph.HE].
- [4] S. Mereghetti, V. Savchenko, C. Ferrigno, D. Götz, M. Rigoselli, A. Tiengo, A. Bazzano, E. Bozzo, A. Coleiro, T. J. L. Courvoisier, M. Doyle, A. Goldwurm, L. Hanlon, E. Jourdain, A. von Kienlin, A. Lu-

tovinov, A. Martin-Carrillo, S. Molkov, L. Natalucci, F. Onori, F. Panessa, J. Rodi, J. Rodriguez, C. Sánchez-Fernández, R. Sunyaev, and P. Ubertini, *ApJ* **898**, L29 (2020), arXiv:2005.06335 [astro-ph.HE].

[5] A. A. Galeev and V. N. Oraevskii, *Soviet Physics Doklady* **7**, 988 (1963).

[6] A. Barnes, *Physics of Fluids* **9**, 1483 (1966).

[7] A. Barnes and R. J. Hung, *Journal of Plasma Physics* **8**, 197 (1972).

[8] J. Derby, N. F., *ApJ* **224**, 1013 (1978).

[9] B. Inhester, *J. Geophys. Res.* **95**, 10525 (1990).

[10] V. Jayanti and J. V. Hollweg, *J. Geophys. Res.* **98**, 13247 (1993).

[11] J. V. Hollweg, *J. Geophys. Res.* **99**, 23431 (1994).

[12] L. Del Zanna, M. Velli, and P. Londrillo, *A&A* **367**, 705 (2001).

[13] Y. Nariyuki and T. Hada, *Physics of Plasmas* **13**, 124501 (2006), arXiv:physics/0608306 [physics.plasm-ph].

[14] L. Del Zanna, L. Matteini, S. Landi, A. Verdini, and M. Velli, *Journal of Plasma Physics* **81**, 325810102 (2015), arXiv:1407.5851 [astro-ph.SR].

[15] M. Shi, H. Li, C. Xiao, and X. Wang, *ApJ* **842**, 63 (2017), arXiv:1705.03829 [physics.space-ph].

[16] Y. Nariyuki, *Reviews of Modern Plasma Physics* **6**, 22 (2022).

[17] Y. Lyubarsky, *ApJ* **682**, 1443 (2008), arXiv:0804.2069 [astro-ph].

[18] M. Iwamoto, E. Sobacchi, and L. Sironi, *MNRAS* **522**, 2133 (2023), arXiv:2304.03577 [astro-ph.HE].

[19] W. Ishizaki and K. Ioka, *Phys. Rev. E* **110**, 015205 (2024), arXiv:2404.15689 [astro-ph.HE].

[20] C. E. Max, *Physics of Fluids* **16**, 1480 (1973).

[21] R. D. Blandford and E. T. Scharlemann, *Ap&SS* **36**, 303 (1975).

[22] R. D. Blandford and E. T. Scharlemann, *MNRAS* **174**, 59 (1976).

[23] D. B. Wilson and M. J. Rees, *MNRAS* **185**, 297 (1978).

[24] D. B. Wilson, *MNRAS* **200**, 881 (1982).

[25] Y. E. Lyubarskii and S. A. Petrova, *Astronomy Letters* **22**, 399 (1996).

[26] P. Kaw, G. Schmidt, and T. Wilcox, *Physics of Fluids* **16**, 1522 (1973).

[27] C. E. Max, J. Arons, and A. B. Langdon, *Phys. Rev. Lett.* **33**, 209 (1974).

[28] D. W. Forslund, J. M. Kindel, and E. L. Lindman, *Physics of Fluids* **18**, 1002 (1975).

[29] M. Tabak, J. Hammer, M. E. Glinsky, W. L. Kruer, S. C. Wilks, J. Woodworth, E. M. Campbell, M. D. Perry, and R. J. Mason, *Physics of Plasmas* **1**, 1626 (1994).

[30] C. Deutsch, H. Furukawa, K. Mima, M. Murakami, and K. Nishihara, *Phys. Rev. Lett.* **77**, 2483 (1996).

[31] T. Kwan and J. M. Dawson, *Physics of Fluids* **22**, 1089 (1979).

[32] L. Friedland, *Physics of Fluids* **23**, 2376 (1980).

[33] A. M. Beloborodov, *ApJ* **922**, L7 (2021), arXiv:2108.07881 [astro-ph.HE].

[34] A. M. Beloborodov, *Phys. Rev. Lett.* **128**, 255003 (2022), arXiv:2108.05464 [astro-ph.HE].

[35] Y. Qu, P. Kumar, and B. Zhang, *MNRAS* **515**, 2020 (2022), arXiv:2204.10953 [astro-ph.HE].

[36] A. Y. Chen, Y. Yuan, X. Li, and J. F. Mahlmann, arXiv e-prints , arXiv:2210.13506 (2022), arXiv:2210.13506 [astro-ph.HE].

[37] A. M. Beloborodov, *ApJ* **959**, 34 (2023), arXiv:2210.13509 [astro-ph.HE].

[38] A. M. Beloborodov, *ApJ* **975**, 223 (2024), arXiv:2307.12182 [astro-ph.HE].

[39] Y.-C. Huang and Z.-G. Dai, *ApJ* **975**, 226 (2024), arXiv:2410.04065 [astro-ph.HE].

[40] R. Nishiura and K. Ioka, *Phys. Rev. D* **109**, 043048 (2024), arXiv:2310.02306 [astro-ph.HE].

[41] E. Sobacchi, M. Iwamoto, L. Sironi, and T. Piran, *A&A* **690**, A332 (2024), arXiv:2409.10732 [astro-ph.HE].

[42] R. Nishiura, S. F. Kamijima, M. Iwamoto, and K. Ioka, *Phys. Rev. D* **111**, 063055 (2025), arXiv:2411.00936 [astro-ph.HE].

[43] B. C. CHIME/FRB Collaboration, Andersen, K. Bandura, M. Bhardwaj, P. J. Boyle, C. Brar, D. Breitman, T. Cassanelli, S. Chatterjee, P. Chawla, J.-F. Cliche, D. Cubranic, A. P. Curtin, M. Deng, M. Dobbs, F. A. Dong, E. Fonseca, B. M. Gaensler, U. Giri, D. C. Good, A. S. Hill, A. Josephy, J. F. Kaczmarek, Z. Kader, J. Kania, V. M. Kaspi, C. Leung, D. Z. Li, H.-H. Lin, K. W. Masui, R. McKinven, J. Mena-Parra, M. Merryfield, B. W. Meyers, D. Michilli, A. Naidu, L. Newburgh, C. Ng, A. Ordog, C. Patel, A. B. Pearlman, U.-L. Pen, E. Petroff, Z. Pleunis, M. Rafiee-Ravandi, M. Rahman, S. Ransom, A. Renard, P. Sanghavi, P. Scholz, J. R. Shaw, K. Shin, S. R. Siegel, S. Singh, K. Smith, I. Stairs, C. M. Tan, S. P. Tendulkar, K. Vanderlinde, D. V. Wiebe, D. Wulf, and A. Zwaniga, *Nature* **607**, 256 (2022), arXiv:2107.08463 [astro-ph.HE].

[44] K. Nimmo, J. W. T. Hessels, F. Kirsten, A. Keimpema, J. M. Cordes, M. P. Snelders, D. M. Hewitt, R. Karuppusamy, A. M. Archibald, V. Bezrukova, M. Bhardwaj, R. Blaauw, S. T. Buttaccio, T. Cassanelli, J. E. Conway, A. Corongiu, R. Feiler, E. Fonseca, O. Forssén, M. Gawroński, M. Giroletti, M. A. Kharinov, C. Leung, M. Lindqvist, G. Maccaferri, B. Marcote, K. W. Masui, R. McKinven, A. Melnikov, D. Michilli, A. G. Mikhailov, C. Ng, A. Orbidan, O. S. Ould-Boukattine, Z. Paragi, A. B. Pearlman, E. Petroff, M. Rahman, P. Scholz, K. Shin, K. M. Smith, I. H. Stairs, G. Surcis, S. P. Tendulkar, W. Vlemmings, N. Wang, J. Yang, and J. P. Yuan, *Nature Astronomy* **6**, 393 (2022), arXiv:2105.11446 [astro-ph.HE].

[45] K. Nimmo, Z. Pleunis, P. Beniamini, P. Kumar, A. E. Lanman, D. Z. Li, R. Main, M. W. Sammons, S. Andrew, M. Bhardwaj, S. Chatterjee, A. P. Curtin, E. Fonseca, B. M. Gaensler, R. C. Joseph, Z. Kader, V. M. Kaspi, M. Lazda, C. Leung, K. W. Masui, R. McKinven, D. Michilli, A. Pandhi, A. B. Pearlman, M. Rafiee-Ravandi, K. R. Sand, K. Shin, K. Smith, and I. H. Stairs, *Nature* **637**, 48 (2025), arXiv:2406.11053 [astro-ph.HE].

[46] G. S. S. Sweeney and P. Stewart, *A&A* **66**, 139 (1978).

[47] V. Muñoz and L. Gomberoff, *Phys. Rev. E* **57**, 994 (1998).

[48] G. Z. Machabeli, S. V. Vladimirov, and D. B. Melrose, *Phys. Rev. E* **59**, 4552 (1999).

[49] S. Matsukiyo and T. Hada, *Phys. Rev. E* **67**, 046406 (2003).

[50] V. Muñoz, T. Hada, and S. Matsukiyo, *Earth, Planets and Space* **58**, 1213 (2006).

[51] R. A. López, F. A. Asenjo, V. Muñoz, and J. Alejandro Valdivia, *Physics of Plasmas* **19**, 082104 (2012).

[52] R. A. López, V. Muñoz, A. F. Viñas, and J. Alejandro Valdivia, *Physics of Plasmas* **21**, 032102 (2014).

[53] V. Muñoz, F. A. Asenjo, M. Domínguez, R. A. López,

J. A. Valdivia, A. Viñas, and T. Hada, *Nonlinear Processes in Geophysics* **21**, 217 (2014).

[54] R. Nishiura, S. F. Kamijima, and K. Ioka, arXiv e-prints , arXiv:2510.12869 (2025), arXiv:2510.12869 [astro-ph.HE].

[55] S. F. Kamijima, R. Nishiura, M. Iwamoto, and K. Ioka, arXiv e-prints , arXiv:2601.01169 (2026), arXiv:2601.01169 [astro-ph.HE].

[56] R. Klíma, *Czechoslovak Journal of Physics* **18**, 1280 (1968).

[57] J. R. Cary and A. N. Kaufman, *Phys. Rev. Lett.* **39**, 402 (1977).

[58] J. R. Cary and A. N. Kaufman, *Physics of Fluids* **24**, 1238 (1981).

[59] T. Hatori and H. Washimi, *Phys. Rev. Lett.* **46**, 240 (1981).

[60] N. C. Lee and G. K. Parks, *The Physics of Fluids* **26**, 724 (1983), https://pubs.aip.org/aip/pfl/article-pdf/26/3/724/12747913/724_1_online.pdf.

[61] N. C. Lee and G. K. Parks, *Geophys. Res. Lett.* **23**, 327 (1996).

[62] R. Z. Sagdeev and A. A. Galeev, *Nonlinear Plasma Theory* (1969).

[63] D. B. Melrose, *Reviews of Modern Plasma Physics* **1**, 5 (2017), arXiv:1707.02009 [physics.plasm-ph].

[64] Z. Pleunis, D. C. Good, V. M. Kaspi, R. Mckinven, S. M. Ransom, P. Scholz, K. Bandura, M. Bhardwaj, P. J. Boyle, C. Brar, T. Cassanelli, P. Chawla, F. (Adam) Dong, E. Fonseca, B. M. Gaensler, A. Josephy, J. F. Kaczmarek, C. Leung, H.-H. Lin, K. W. Masui, J. Mena-Parra, D. Michilli, C. Ng, C. Patel, M. Rafiee-Ravandi, M. Rahman, P. Sanghavi, K. Shin, K. M. Smith, I. H. Stairs, and S. P. Tendulkar, *ApJ* **923**, 1 (2021), arXiv:2106.04356 [astro-ph.HE].

[65] J. J. Thomson, W. L. Kruer, S. E. Bodner, and J. S. DeGroot, *Physics of Fluids* **17**, 849 (1974).

[66] C. Thompson, R. D. Blandford, C. R. Evans, and E. S. Phinney, *ApJ* **422**, 304 (1994).

[67] W. Kruer, *The Physics Of Laser Plasma Interactions* (CRC Press, 2019).

[68] B. Brandão, J. E. Santos, R. M. G. M. Trines, R. Birmingham, and L. O. Silva, *Plasma Physics and Controlled Fusion* **63**, 094003 (2021), arXiv:2104.04097 [physics.plasm-ph].

[69] Y. Zhao, S.-M. Weng, H.-H. Ma, X.-J. Bai, and Z.-M. Sheng, *Reviews of Modern Plasma Physics* **7**, 1 (2023).

[70] P. Goldreich and W. H. Julian, *ApJ* **157**, 869 (1969).

[71] B. M. Gaensler, C. Kouveliotou, J. D. Gelfand, G. B. Taylor, D. Eichler, R. A. M. J. Wijers, J. Granot, E. Ramirez-Ruiz, Y. E. Lyubarsky, R. W. Hunstead, D. Campbell-Wilson, A. J. van der Horst, M. A. McLaughlin, R. P. Fender, M. A. Garrett, K. J. Newton-McGee, D. M. Palmer, N. Gehrels, and P. M. Woods, *Nature* **434**, 1104 (2005), arXiv:astro-ph/0502393 [astro-ph].

[72] J. D. Gelfand, Y. E. Lyubarsky, D. Eichler, B. M. Gaensler, G. B. Taylor, J. Granot, K. J. Newton-McGee, E. Ramirez-Ruiz, C. Kouveliotou, and R. A. M. J. Wijers, *ApJ* **634**, L89 (2005), arXiv:astro-ph/0503269 [astro-ph].

[73] J. Granot, E. Ramirez-Ruiz, G. B. Taylor, D. Eichler, Y. E. Lyubarsky, R. A. M. J. Wijers, B. M. Gaensler, J. D. Gelfand, and C. Kouveliotou, *ApJ* **638**, 391 (2006), arXiv:astro-ph/0503251 [astro-ph].

[74] C. Thompson and R. C. Duncan, *MNRAS* **275**, 255 (1995).

[75] K. Ioka, *ApJ* **904**, L15 (2020), arXiv:2008.01114 [astro-ph.HE].

[76] T. Wada and K. Ioka, *MNRAS* **519**, 4094 (2023), arXiv:2208.14320 [astro-ph.HE].

[77] Y.-H. Yang, B.-B. Zhang, L. Lin, B. Zhang, G.-Q. Zhang, Y.-S. Yang, Z.-L. Tu, J.-H. Zou, H.-Y. Ye, F.-Y. Wang, and Z.-G. Dai, *ApJ* **906**, L12 (2021), arXiv:2009.10342 [astro-ph.HE].

[78] F. Kirsten, M. P. Snelders, M. Jenkins, K. Nimmo, J. van den Eijnden, J. W. T. Hessels, M. P. Gawroński, and J. Yang, *Nature Astronomy* **5**, 414 (2021), arXiv:2007.05101 [astro-ph.HE].

[79] C. Thompson and O. Blaes, *Phys. Rev. D* **57**, 3219 (1998).

[80] X. Li, J. Zrake, and A. M. Beloborodov, *ApJ* **881**, 13 (2019), arXiv:1810.10493 [astro-ph.HE].

[81] Y. Lyubarsky, *MNRAS* **483**, 1731 (2019), arXiv:1811.11122 [astro-ph.HE].

[82] E. Golbraikh and Y. Lyubarsky, *ApJ* **957**, 102 (2023), arXiv:2309.09218 [astro-ph.HE].

[83] V. M. Lipunov and I. E. Panchenko, *A&A* **312**, 937 (1996), arXiv:astro-ph/9608155 [astro-ph].

[84] K. Ioka and K. Taniguchi, *ApJ* **537**, 327 (2000), arXiv:astro-ph/0001218 [astro-ph].

[85] B. M. S. Hansen and M. Lyutikov, *MNRAS* **322**, 695 (2001), arXiv:astro-ph/0003218 [astro-ph].

[86] T. Wada, M. Shibata, and K. Ioka, *Progress of Theoretical and Experimental Physics* **2020**, 103E01 (2020), arXiv:2008.04661 [astro-ph.HE].

End Matter

which can be applied in the regime $\omega_0 \ll \omega_p \ll \omega_c$.

Neutral Mode: Linear Growth Rates for a Monochromatic Incident Wave

The maximum linear growth rate of the neutral mode for a monochromatic incident wave is (see Eq. (66) in [54])

$$(t_{\text{neutral}}^{\text{coh}})^{-1} \sim \begin{cases} \sqrt{\frac{\pi}{32e}} \frac{a_e^2 \omega_p^2}{\omega_0} \frac{m_e c^2}{k_B T_e} \left(\frac{\omega_0}{\omega_c}\right)^4 \left(1 + \frac{\omega_p^2}{\omega_c^2}\right)^{-1}, \\ a_e \frac{\omega_0}{\omega_c} \ll \left(a_e \frac{\omega_0}{\omega_c}\right)_{\text{trans}}^{\text{coh}}, \\ \sqrt{3} \left(\frac{a_e^2 \omega_p^2 \omega_0}{2}\right)^{\frac{1}{3}} \left(\frac{\omega_0}{\omega_c}\right)^{\frac{4}{3}}, \\ \left(a_e \frac{\omega_0}{\omega_c}\right)_{\text{trans}}^{\text{coh}} \ll a_e \frac{\omega_0}{\omega_c} \ll 1, \end{cases} \quad (\text{A.7})$$

where the upper expression corresponds to ICS, and the lower one to SBS. The transition point is

$$\left(a_e \frac{\omega_0}{\omega_c}\right)_{\text{trans}}^{\text{coh}} \simeq 4.4 \frac{\omega_c}{\omega_p} \left(\frac{k_B T_e}{m_e c^2}\right)^{\frac{3}{4}} \left(1 + \frac{\omega_p^2}{\omega_c^2}\right)^{\frac{3}{4}}. \quad (\text{A.8})$$

Neutral mode: Linear Growth Rates for a Broadband Incident Wave

For a broadband incident wave with bandwidth $\Delta\omega$, the maximum linear growth rate of the neutral mode is (see Eq. (130) in [54])

$$(t_{\text{neutral}}^{\text{broad}})^{-1} \sim \begin{cases} \pi \left(a_e \frac{\omega_p}{\omega_0}\right)^2 \left(\frac{\omega_0}{\omega_c}\right)^4 \left(\frac{\omega_0}{\Delta\omega}\right)^2 \omega_0, \\ a_e \frac{\omega_0}{\omega_c} \ll \left(a_e \frac{\omega_0}{\omega_c}\right)_{\text{trans}}^{\text{broad}}, \\ \frac{3}{2^{\frac{3}{2}}} \left(a_e \frac{\omega_p}{\omega_0}\right)^{\frac{4}{3}} \left(\frac{\omega_0}{\omega_c}\right)^{\frac{8}{3}} \frac{\omega_0}{\Delta\omega} \omega_0, \\ \left(a_e \frac{\omega_0}{\omega_c}\right)_{\text{trans}}^{\text{broad}} \ll a_e \frac{\omega_0}{\omega_c} \ll 1, \end{cases} \quad (\text{A.9})$$

where the upper expression corresponds to ICS, and the lower one to SBS. The transition point is

$$\left(a_e \frac{\omega_0}{\omega_c}\right)_{\text{trans}}^{\text{broad}} \sim 4.7 \times 10^{-1} \frac{\omega_c}{\omega_p} \left(\frac{\Delta\omega}{\omega_0}\right)^{\frac{3}{2}}. \quad (\text{A.10})$$

Charged mode: Linear Growth Rates for a Broadband Incident Wave

In the charged mode, ICS with Debye screening yields the maximum linear growth rate (see Eq. (133) in [54])

$$(t_{\text{charged}}^{\text{broad}})^{-1} \sim \frac{\pi}{4} \left(\frac{\omega_0}{\omega_c}\right)^2 \left(1 + \frac{\omega_p^2}{\omega_c^2}\right)^2 \frac{\omega_p^2 a_e^2}{\omega_0} \times \left(\frac{8k_B T_e}{m_e c^2}\right)^2 \left(\frac{\omega_0}{\omega_p}\right)^4 \left(\frac{\omega_0}{\Delta\omega}\right)^2, \quad (\text{A.11})$$